Accelerated Iterative Method for Solving Steady Solutions of Linearized Atmospheric Models

Masahiro Watanabe[1]

Fei-fei Jin[2]

Lin-lin Pan[2]

1: Faculty of Environmental Earth Science, Hokkaido University

2: Department of Meteorology, Florida State University

Submitted to JAS

September 7, 2005

Corresponding authors:

M. Watanabe, Faculty of Environmental Earth Science, Hokkaido University

Nishi 5 Kita 10, Sapporo, Hokkaido 060-0810, Japan (E-mail: hiro@ees.hokudai.ac.jp)

F.-F. Jin, Department of Meteorology, Florida State University

Love Bldg, Tallahassee, FL32306-4520, USA (E-mail: jff@met.fsu.edu)

ABSTRACT

A new approach, referred to as the accelerated iterative method (AIM), is developed for solving steady atmospheric response under zonally varying basic state. The linear dynamical operator is first divided into two parts, which are associated with the zonally symmetric and asymmetric components of the basic state, respectively. For ensuring the accelerated asymptotic convergence of iterative procedure for the true solution, the two parts of the operator are modified by adding and subtracting an identical arbitrary "accelerating" operator. AIM is shown to be not only efficient but also applicable for solving a steady atmospheric response of high-resolution baroclinic model linearized with a zonally varying basic state. A preliminary application of AIM to the baroclinic model linearized about the observed winter (December-February) climatology is also presented. A series of steady responses forced by the diabatic heating and transient eddy forcing both estimated from reanalysis data for individual winter during 1960-2002 captures a certain part of the observed interannual variability in dominant teleconnections such as the North Atlantic Oscillation and the Pacific/North America pattern. Thus AIM is a useful tool for the diagnostic studies of the low-frequency variability of the atmosphere.

1. Introduction

Monthly or seasonal mean anomalies in the large-scale atmospheric circulation are central to the interannual climate variability. Regardless of their origin, either forced by external forcing or generated through internal processes of the atmosphere, the spatial structure prevailing in such time-mean atmospheric anomalies has been classified into several teleconnection patterns (Wallace and Gutzler 1981; Barnston and Livezey 1987; Kushnir and Wallace 1989; among others). Understanding the generation and maintenance mechanisms of the teleconnection pattern is still an ongoing research effort (Wallace 2000; Hurrell et al. 2003; references therein).

In numerous studies, linearized atmospheric models are shown to be a useful tool to elucidate dynamical processes of the time-mean atmospheric anomalies. In particular, the so-called linear baroclinic model (LBM) that consists of primitive equations linearized about the climatological mean state has been developed by several research groups in order to reproduce and furthermore attribute the anomalies in the global atmosphere. This approach leaves out important questions regarding the dynamics for the observed climatological state; nevertheless, the LBMs are capable enough of capturing the observed teleconnection patterns. In the classic paper of Hoskins and Karoly (1981), steady solutions forced by idealized thermal and orographic forcing are solved based on the 5-level LBM. This study provides insights into the energy propagation of stationary Rossby waves and their association with the extratropical circulation anomalies observed during El Niño, often referred to as the Pacific/North American (PNA) pattern (e.g., Horel and Wallace 1981). When the primitive equations are linearized about a zonally *uniform* state, as in Hoskins and Karoly (1981), the forced solution can be separately solved for each zonal wavenumber.

Because of the convenience, this type of model, called the stationary wave model (SWM), is widely used to simulate either anomalous or climatological stationary waves (see review by Held et al. 2002).

By examining steady solutions under the zonally *varying* basic state, it gradually became clear that the climatological zonal asymmetry in the basic state is crucially important for simulating the anomalous atmospheric circulation (Branstator 1990; Ting and Lau 1993; Ting and Sardeshmukh 1993; DeWeaver and Nigam 2000; Peng and Robinson 2001). Branstator (1990) demonstrated that the steady responses have a preferred structure under the 3D basic state even if the forcing is spatially random. Some of the prevailing patterns found in his LBM are quite similar to the patterns of dominant circulation anomalies identified in a general circulation model (GCM) about which the LBM is linearized, indicating that the coupling between the atmospheric anomaly and the climatological zonal asymmetry is one of the major sources for the large-scale, low-frequency variability of the extratropical atmosphere. Watanabe and Jin (2004) carried out a similar but more sophisticated analysis of the singular vectors to the LBM employing the observed winter 3D climatology as the basic state, showing that some of the dominant teleconnections may be regarded as near-neutral dynamical mode arising from the zonally asymmetric mean state.

When using the LBM with non-zonal basic states, we confront one technical, but critical as well, obstacle; the linear dynamical operator becomes huge to be solved directly. Therefore most of the previous studies in which steady responses are solved by the matrix inversion technique adopt a coarse spatial resolution of, for example, zonal wavenumber up to either 15 or 21 and vertical levels less than 10 (Navarra 1990; Branstator 1990; Ting and Held 1990; Ting and Lau 1993; Watanabe and Kimoto 2000).

This reduction in spatial dimension is often justified by referring to the observed seasonal mean anomalies dominated by planetary-scale components. However, the forcing in many cases has much finer structure, and the small-scale eddies forced by it can modify large-scale eddies via coupling with the zonal asymmetry in the basic state.

There are at least two different ways to be free from the above dimensional constraint: one is to simply integrate the model in time (Hall and Sardeshmukh 1998; Peng and Whitaker 1999; Peng and Robinson 2001). While the time integration approach has an advantage that the nonlinear model can be treated in the same framework (Jin and Hoskins 1995; Ting and Yu 1998), it may not be very efficient computationally. Another, in which the present work is categorized, is to solve the linear operator matrix with help of advanced algorithms. For example, in Branstator (1992) steady responses are solved using the out-of-core algorithm which saves the computer memory. On the other hand, DeWeaver and Nigam (2000) parallelized the model, which is quite efficient in solving a large matrix by using the scalable routines. In the present study, an alternative method is explored following the relaxation idea. We pay attention to the fact that the SWM is solved much easier than the full LBM, so that attempt to construct a scheme that the steady response under zonally symmetric basic state is first calculated by the direct method then correcting it iteratively such as to satisfy a dynamical balance with the zonally asymmetric state. Throughout the paper, the scheme is referred to as the accelerated iterative method (AIM) since a modification is made to the linear operator for a fast convergence of the numerical iteration.

This paper is organized as follows. In the next section, mathematical basis of AIM and the linearized atmospheric models to which AIM is applied are described. In section 3, the characteristics of AIM in terms of convergence, accuracy and comparison

with other methods are examined using the barotropic model. AIM is then applied to the LBM in section 4, aiming at hindcasting the observed interannual variability in the teleconnection patterns. Section 5 gives summary and discussion.

2. Models and methodology

a. Principle of AIM

A general expression of the time evolution of linear perturbation is written in the matrix form

$$\frac{\mathrm{d}}{\mathrm{d}t}\mathbf{X}_a + \mathbf{L}(\mathbf{X}_c)\mathbf{X}_a = \mathbf{F} \quad , \tag{1}$$

where $\mathbf{X}_a$ denotes a perturbation state vector of the atmosphere, $\mathbf{F}$ the external forcing, and $\mathbf{L}$ the dynamical operator of the governing equations as a linear function of basic state $\mathbf{X}_c$. For steady problem where tendency term can be ignored, with a given forcing $\mathbf{X}_a$ is obtained by inverting $\mathbf{L}$ as $\mathbf{X}_a = \mathbf{L}^{-1}\mathbf{F}$, which is easy for a small matrix such as in the barotropic model. As mentioned in the introduction, however, the size of $\mathbf{L}$ exceeds 3×10^4 for LBM even with a coarse resolution of T21 and vertical 20 levels, which is hardly implemented. To develop AIM, we divide the basic state into the zonally symmetric and asymmetric parts, denoted as $\bar{\mathbf{X}}_c$ and $\mathbf{X}_c^*$, respectively.

$$\mathbf{L}_S(\bar{\mathbf{X}}_c)\mathbf{X}_a + \mathbf{L}_A(\mathbf{X}_c^*)\mathbf{X}_a = \mathbf{F} \quad , \tag{2}$$

where $\mathbf{L}_S$ ($\mathbf{L}_A$) is the dynamical operator linearized about $\bar{\mathbf{X}}_c$ ($\mathbf{X}_c^*$). Since $\mathbf{L}_S$ consists of block matrices separated for each zonal wavenumber, it can be easily inverted, consequently an iterative scheme for Eq. (2) may be constructed as

$$\mathbf{X}_a^{\mathrm{n+1}} = -\mathbf{L}_S^{-1}\mathbf{L}_A\mathbf{X}_a^{\mathrm{n}} + \mathbf{L}_S^{-1}\mathbf{F} = \mathbf{M}\mathbf{X}_a^{\mathrm{n}} + \mathbf{G} \quad , \tag{3}$$

where n indicates the iteration step.

Equation (3) has the same form as the conventional Jacobian relaxation, leading to the condition for convergence in terms of the spectral radius of $\mathbf{M}$ (cf. Meurant 1999; Kalnay 2003)

$$\rho(\mathbf{M}) = \max|\sigma_i| < 1 \quad , \tag{4}$$

where the spectral radius ρ is defined by the maximum of the absolute eigenvalues of $\mathbf{M}$, $|\sigma_i|$. As will be shown later, the condition (4) is not generally satisfied for the steady atmospheric problem. Therefore we intend to shrink the eigenspectrum of $\mathbf{M}$ by introducing an accelerating operator matrix denoted as $\mathbf{R}$ to Eq. (2):

$$(\mathbf{L}_S + \mathbf{R})\mathbf{X}_a + (\mathbf{L}_A - \mathbf{R})\mathbf{X}_a = \mathbf{F} \quad . \tag{5}$$

A modified iterative scheme becomes

$$\mathbf{X}_a^{n+1} = (\mathbf{R} + \mathbf{L}_S)^{-1}(\mathbf{R} - \mathbf{L}_A)\mathbf{X}_a^n + (\mathbf{R} + \mathbf{L}_S)^{-1}\mathbf{F} \quad , \tag{6}$$

with $\mathbf{X}_a^0 = 0$. The acceleration matrix $\mathbf{R}$ in Eq. (6) is chosen to ensure

$$\rho(\mathbf{M}^*) < 1 \quad , \tag{7}$$

where the iteration matrix $\mathbf{M}^*$ is defined as

$$\mathbf{M}^* \equiv (\mathbf{R} + \mathbf{L}_S)^{-1}(\mathbf{R} - \mathbf{L}_A) \quad , \tag{8}$$

The choice of the form of $\mathbf{R}$ in Eq. (8) is the crucial part of AIM. The primary criterion is that real parts of the eigenvalues of $\mathbf{R}$ are all positive, which is proved as follows. When the norm of $\mathbf{R}$ is sufficiently large, we will have the following first order Taylor expansion to $\mathbf{M}^*$:

$$\mathbf{M}^* \approx \mathbf{I} - \mathbf{R}^{-1}\mathbf{L} \quad , \tag{9}$$

where $\mathbf{I}$ denotes an identity matrix. Since all the eigenvalues of $\mathbf{R}$ are of positive real

parts by definition, it turns out from Eq. (9) that the spectral radius $\rho(\mathbf{M}^*)$ is always smaller than 1 if the real part of eigenvalues of $\mathbf{L}$ is all positive, i.e., no instability occurs. Thus when the operator $\mathbf{L}$ is dynamically stable or near neutral, the scheme (6) is guaranteed to converge.

Suppose a simple case of $\mathbf{R} = \mathbf{I}/\Delta t$, where Δt is the time interval for integrating Eq.(1). With this form of $\mathbf{R}$ which satisfies the above criterion, Eq. (6) can be regarded as a kind of semi-implicit scheme. It is also found intuitively that, for "acceleration" in "time stepping", larger (smaller) Δt can be used for large-scale (small-scale) waves. From this point of view, it would be obvious that, if we choose a scale-dependent $\mathbf{R}$, it truly serves as acceleration in the scheme (6) to achieve a steady solution through rescaling the timescales differently for different wave components in the spectral domain.

Furthermore, for computational efficiency, it is required that $\mathbf{R}$ can be decomposed into block matrices so that $\mathbf{R} + \mathbf{L}_S$ is inverted separately for each zonal wavenumber. For these reasons, we take the following form of $\mathbf{R}$:

$$\mathbf{R} = \gamma \mathbf{D} \quad , \tag{10}$$

where γ is a parameter while $\mathbf{D}$ is the matrix containing a scale-selective diffusion employed in the model. Note that we anticipate that this method is applied to spectral models, so that $\mathbf{D}$ becomes the diagonal matrix. From the above choice of $\mathbf{R}$ in Eq. (10), it can be inferred that there is an optimal value of γ for fast convergence. When γ is zero, Eq. (6) reduces to Eq. (3) which may diverge. When γ is too large, the spectral radius of $\mathbf{M}^*$ will be close to 1, resulting in the convergence very slow. It will be shown in the next section that indeed there is a certain choice of the moderate value of γ that

makes the scheme (6) not only converge but also converge rapidly. Furthermore, when implementing the scheme (6), we only need to calculate and invert the block matrices of $\mathbf{R}+\mathbf{L}_S$, which is done for each zonal wavenumber separately. There is no need to obtain and keep the large matrix $\mathbf{L}_A$, rather we use the rhs terms of the model equations to directly calculate the vector $(\mathbf{R}-\mathbf{L}_A)\mathbf{X}_a^{\mathrm{n}}+\mathbf{F}$. Thus each iteration requires nearly the same amount of calculation as integrating the model one step forward. As long as the block matrices are inverted beforehand, the iteration does not involve any large matrix operations and thus AIM composed of Eqs. (6) and (10) is highly efficient.

b. Linear atmospheric models

We use two different atmospheric models in this study: one simplified hence easy to handle and the other complicated hence more realistic but computationally expensive. The former follows a barotropic vorticity equation linearized about the observed 300 hPa mean flow whereas the latter is the LBM which we have developed previously (Watanabe and Kimoto 2000, 2001; Watanabe and Jin 2004). Both models are represented by the spherical harmonics and to solve the global atmospheric response to prescribed forcing.

The barotropic model is used to examine the characteristics of AIM, for example, the convergence, efficiency, and resolution dependence, which are presented in the next section. For this purpose, the steady streamfunction response to an idealized tropical forcing is repeatedly solved with the resolution of T21, T42, T63, and T106, respectively. The model employs the biharmonic horizontal diffusion, corresponding to $\mathbf{D}$ in Eq. (10), whose coefficients depend on the resolution (see Table 1) as well as the

Rayleigh friction with the damping timescale of 10 days in order to prevent the instability. The model basic state is derived from the winter (December-February) mean climatology of the NCEP-NCAR reanalysis data during 1949-1999 (Kalnay et al. 1996) while the idealized vorticity source which mimics the anomalous divergent forcing during El Niño follows Branstator (1985). Note that the characteristics of AIM crucially depend on the dynamical operator but not on the forcing structure.

LBM is based on an exactly linearized set of equations for vorticity (ζ), divergence (D), temperature (T), and logarithm of surface pressure ($\pi=\ln Ps$). The model variables are expressed horizontally by the spherical harmonics as in the barotropic model but the truncation is fixed at T42 while the finite difference is used for the vertical discretization which is fixed at 20 sigma levels. The model includes three dissipation terms: a biharmonic horizontal diffusion to ζ, D, and T, weak vertical diffusion (damping timescale of 1000 days) to remove a vertical noise arising from finite difference, and the Newtonian damping and Rayleigh friction as represented by a linear drag. The drag coefficients have a damping timescale of 0.5 day at the lowest four levels ($\sigma \geq 0.9$), which mimic the turbulent fluxes and the surface friction, and also at the topmost two levels ($\sigma < 0.03$) that prevent a false wave reflection at the boundary. Inbetween, the $(20 \text{ days})^{-1}$ damping is applied, which does not seriously affect the amplitude and structure of the response. The boundary layer damping adopted here roughly follows the mixing coefficients evaluated with the Mellor-Yamada closure in the CCSR/NIES AGCM, based on which we have developed LBM, and is strong enough to neutralize baroclinic instability waves in the system (Hall and Sardeshmukh 1998). When applying AIM to the model, the coefficient of the horizontal diffusion is important parameter, which is fixed at a relatively large value corresponding to the

damping timescale of 2 hours for the smallest wave. The basic state of LBM is adopted from the winter 3D climatology of the ECMWF reanalysis data (ERA40) during 1961-1990 (Kållberg et al. 2004). There is no particular reason that we use the different reanalysis data to the barotropic and baroclinic models except that ERA40 has finer vertical resolution.

The forcing given to LBM consists of the diabatic heating anomaly and the anomalous transient eddy forcing: the former is obtained as the residual of the thermodynamic equation (cf. Yanai et al. 1992) while the latter is represented by the convergence of horizontal vorticity fluxes due to submonthly disturbances, both of which are calculated using the 6 hourly ERA40 data during 1960-2002. After the winter anomalies of these forcing terms have been calculated, they are interpolated onto the model grid space. It should be noted that both the diabatic heating and eddy vorticity forcing is smoothly filtered out poleward of 80 degrees since they have some erroneous features near the pole. The convergence of transient eddy heat fluxes is not included in the forcing since it is known to work as thermal diffusion (Ting and Lau 1993) hence approximated by the stronger horizontal diffusion employed in the model.

3. Verification of AIM using the barotropic model

a. Measures of convergence

In this section, the extent to which AIM is efficient in obtaining the steady forced solution is examined using the barotropic model. The approximate solution at each iteration step is compared to the true response that has been calculated by the conventional matrix inversion in advance. The criterion for convergence, ε, is defined here by the RMS error between the true and AIM solutions,

$$\varepsilon^{n} = \left\| \mathbf{X} - \mathbf{X}^{n} \right\| / \left\| \mathbf{X} - \mathbf{X}^{1} \right\| \quad , \tag{11}$$

where $\mathbf{X}$ denotes the true solution, represented by the anomalous streamfunction in case of the barotropic model, whereas $\mathbf{X}^{n}$ is the AIM solution at nth step. In order to eliminate the dependence of ε on the model resolution and magnitude of forcing, the RMS error is normalized by the error at the first step $\mathbf{X}^{1}$. For the huge matrix which cannot be solved directly, as in the case of LBM, another measure for convergence which is evaluated without knowledge of the true solution is provided by the normalized differential norm,

$$\lambda^{n} = \left\| \mathbf{X}^{n} - \mathbf{X}^{n-1} \right\| / \left\| \mathbf{X}^{2} - \mathbf{X}^{1} \right\| \quad (n>1) \quad . \tag{12}$$

b. Basic properties of AIM

Figure 1 shows the RMS error ratio defined by Eq. (11) for the T21 barotropic model response. The values of ε for varying parameter γ (from 1 to 5) are plotted up to n=100. For $\gamma = 0$, which corresponds to $\mathbf{M}^{*} = \mathbf{M}$, the error immediately increases exponentially while for $\gamma = 1$ or 2, ε once decreases but gradually starts increasing, leading to the AIM solution blowing up. When γ is increased to 4, the error continuously decreases and reaches almost 10^{-5} at n=100. A similar evolution is found for $\gamma = 5$ but the convergence is slightly slower, therefore it is found that AIM solutions for $\gamma \geq 4$ converge, with $\gamma = 4$ the best choice in this case. It is noted that the error reduction is not exactly monotonic due to an oscillatory behavior with small amplitude. This fluctuation disappears when $\mathbf{R}$ includes the linear drag as well, which, however, results in the slower convergence (not shown).

It has been explained in section 2a that the spectral radius of $\mathbf{M}^*$ is reduced for larger value of γ thus the convergence property of AIM is guaranteed for sufficiently large γ. This is verified by carrying out the eigenanalysis to $\mathbf{M}^*$ with different values of γ (Fig. 2). A plot of eigenvalues in the complex domain clearly indicates $\rho(\mathbf{M}) > 1$, which is out of the convergence criterion (Fig. 2a). For $\gamma = 1$ the eigenvalue spectrum does not change largely while for $\gamma = 10$ most of eigenvalues reside in the unit circle although $\rho(\mathbf{M}^*)$ is yet larger than 1 (Figs. 2b and 2c). Since $\mathbf{M}^*$ approaches the identity matrix for $\gamma \to \infty$ (cf. Eq.(8)), it is not surprising that for $\gamma = 100$ the eigenvalues are gathered around (0,1) in the complex plane (Fig. 2d). In case of the T42 barotropic model shown in Fig. 2, the best choice of γ is $\gamma = 38$ （cf. Table 1）, when the eigenspectrum is the most shrank toward the origin (not shown).

It is shown in Fig. 1 that, if we allow the 10% (1%) error, only 9 (30) steps are necessary to obtain the steady response for the T21 model (see also Table 1). Efficiency of this convergence rate is compared to other two iterative methods: the conventional time integration and the conjugate gradient (CG) method, familiar one in the Krylov subspace techniques (Greenbaum 1997). The time integration employs the interval of Δt=60 minutes which is determined from the CFL condition. The CG method is suggested to apply to a symmetric matrix, so that the transpose of $\mathbf{L}$ has been multiplied before the iteration. To justify the comparison, both time integration and CG solver adopt the first guess $\mathbf{X}^1$ obtained from AIM. The result in terms of the RMS error ratio is presented in Fig. 3, which shows that, as we expect, AIM is the most efficient scheme. The iteration steps for the steady solution with 10% error are 9 for

AIM, 138 for CG, and 380 for the time integration (roughly 16 days), respectively.

The spatial pattern of the streamfunction response is displayed in Fig. 4a. While there is no preference in the forcing and response structure in the present test, it is well identified that the stationary Rossby waves akin to the PNA and Pacific/South American patterns are emanating from the equator, as has been found in many studies (e.g. Branstator 1985). A first guess for the AIM solution with $\gamma = 4$, shown in Fig. 4b, also reveal such wave trains even though the amplitude is weaker than the true solution. The steady solutions in CG and AIM with the 1% RMS error contained, obtained at n=262 and n=30, respectively, are almost identical to the true response (Figs. 4c and 4d). The overall pattern and amplitude of these approximated solutions are quite similar even with the 10% error (not shown).

c. Dependence on the intrinsic diffusion

In choosing the form of $\mathbf{R}$, we have considered that the scale-selective matrix acts as acceleration of the iteration and then the efficiency is controlled by γ. On the other hand, the inertia of each wave would be dependent on the magnitude of the intrinsic diffusion of the system, i.e., $\mathbf{D}$ in Eq. (10), so that the convergence efficiency of AIM may also be affected by changing $\mathbf{D}$. Specifically, it is reasonable to speculate that the convergence of the AIM solution will be slower (faster) for weaker (stronger) intrinsic diffusion of the dynamical operator. The confirmation is made by evaluating ε in the T21 barotropic model used in Fig. 1 but with the e-folding decay timescale of the horizontal diffusion altered from 1 day to either half a day or 2 days. In both cases the AIM solution is successfully converged with the best choice of γ. The resultant profiles of ε support our speculation as shown in Fig. 5 which reveals that the iteration steps

drastically change when smaller ε is employed to measure the convergence. For $\varepsilon = 0.01$ (1% error), which we think a typical threshold, the necessary iteration is shortened to 19 for stronger diffusion while lengthened to 46 for weaker diffusion.

The result shown in Fig. 5 indicates the convergence rate highly sensitive to the level of intrinsic diffusion in the dynamical operator. At the same time, it may imply that the computational efficiency of AIM remains the same for different spatial resolution as long as the level of diffusion is preserved. This is indeed found to be true, which is evident in the summary of iteration steps for convergence at various resolutions (Fig. 6). In the figure, n for $\varepsilon = 0.01$ calculated with T21, T42, T63, and T106 barotropic models is presented with respect to the three methods. Number of the degrees of freedom (gray line) provides the theoretical maximum of n for CG and AIM. When the diffusion profile is kept fixed at the T21 version, the iteration steps for CG and time integration increase for higher resolution while those for AIM are almost constant (dashed lines in Fig. 6). In this comparison, it is clear that AIM is the most efficient when applying to the highest resolution. While this resolution-independent property is one of the advantages of AIM, this may not be hold in the practical application since the diffusion which has the decay time of 24 hours in T21 corresponds to 1.5 hour in T42, 19 minutes in T63, and only 2.4 minutes in T106! The scale-selective diffusion is, in general, included to remove the enstrophy accumulation near the truncated wavenumber, so that such a strong diffusion does not make sense. When we used more 'plausible' diffusion profile which becomes weaker in higher resolution (see Table 1), the convergence rate of AIM, as well as other two methods, comes to depend on the resolution (solid lines in Fig. 6). Nevertheless, AIM is still shown to be much efficient than CG, and more than one order faster than the time integration, which

gives the relevance of using AIM in the practical calculation.

Before extending AIM to the LBM, the relationship between the RMS error ratio (ε) and the differential norm (λ) is briefly examined in the barotropic framework. Shown in Fig. 7 is the evolution of λ against ε of the AIM solutions at different resolutions. Note that the solutions used here correspond to the solid line in Fig. 6 (i.e. the level of diffusion is not common among four resolutions), but the result is essentially the same for solutions with the common diffusion level. Overall, two measures shown in Fig. 7 are linearly proportional, representing that $\lambda \approx 0.01$ roughly corresponds to the 1-3% error in ε.

4. Application to LBM

a. Simulation of 1997/98 anomalies

The algorithm of AIM was verified in the previous section which shows its considerable efficiency, so that in this section the scheme is applied to LBM. Following Fig. 7, the convergence is evaluated with the threshold of $\lambda = 0.01$[1]. As an example of the LBM diagnosis, 1997/98 winter anomaly field is chosen since it exhibits a large ENSO teleconnection. Figure 8a shows the horizontal wind anomalies at 850 hPa and the geopotential height anomaly at 300 hPa observed during winter 1997/98, illustrating the PNA-like circulation anomaly over the North Pacific in addition to the anomalous westerly (easterly) over the equatorial Pacific (Indian) Ocean. When the T42 20-level LBM with the zonally symmetric basic state is used to calculate the steady linear response to the combined forcing of diabatic heating and transient eddy vorticity fluxes,

[1] The reduction of λ tends to be slow for $\lambda < 0.01$, so that the threshold of $\lambda = 0.01$ greatly saves the computational time while the solution is quite similar to that with one order smaller λ.

the equatorial wind anomaly is reproduced while the PNA-like pattern is distorted (Fig. 8b). On the other hand, the steady response with the zonally asymmetric basic state, obtained by using AIM, reveals cyclonic and anticyclonic anomalies at the correct position over the North Pacific and North America, respectively (Fig. 8c). The difference between Figs. 8b and 8c indicates the significant role of climatological stationary eddies in forming the extratropical teleconnection patterns, as outlined in the introduction. The response pattern is overall quite similar to the observation, but there are discrepancies as well: the circulation anomaly over northern Eurasia is shifted to the west and a false cyclonic anomaly appears off Japan.

The sea level pressure (SLP) response associated with Fig. 8c is compared to the observed SLP anomaly in Fig. 9a-b. Except for the polar caps away 80 degrees, the steady SLP response well captures the major high and low pressure anomalies. It should be noted, however, the magnitude of the SLP response is about half the observed. The cause of this underestimate plausibly comes from the difference in the vertical profile of temperature anomalies. The vertical structure of the observed temperature anomaly at 50°N indicates the maxima occurring near the surface, in particular, over land regions (Fig. 9c). In LBM, such large temperature response is not found because of the strong boundary layer damping which is necessary to prevent the baroclinic instability (Fig. 9d). Following the hydrostatic relation the geopotential height response becomes weak as well, resulting in underestimate of the SLP response which is regarded as the vertical integral of the height response.

b. LBM hindcasts

Despite some discrepancy and insufficient magnitude, LBM solution captures

many features of the observed atmospheric anomalies during 1997/98 El Niño. Encouraged by this result, we attempt to hindcast the anomaly fields for 1960-2002 by solving the steady problem at each winter. For comparison the steady response with the zonally symmetric basic state is also calculated.

The capability of LBM in hindcasting the winter anomaly fields is first evaluated with the standard deviation of the 500 hPa height anomalies (Fig. 10). In observations, three maxima of the height variance are identified over the central North Pacific, Greenland, and north of Siberia (Fig. 10a). The standard deviation in steady height responses under the zonally symmetric basic state shows a pattern not very far from observations, but the locations of maximum variance do not coincide except for the North Pacific (Fig. 10b). It should be noted that the zonally symmetric response has a significant contribution to the variance map, so that the SWM hindcast produces a worse result (not shown). The height standard deviation obtained from the full LBM (Fig. 10c) is improved in terms of the maxima over Greenland and north of Siberia while the maximum over the North Pacific is even shifted eastward. As found in the 1997/98 case, LBM response tends to be weak in the lower troposphere due to boundary layer drag, leading to the standard deviation with the amplitude about half or two third of the observation.

The major task of the LBM hindcast is to examine the extent to which the interannual variability of the dominant teleconnections can be simulated. This is simply investigated by comparing several climate indices: Southern Oscillation Index (SOI), PNA index, and the North Atlantic Oscillation (NAO) index. The SOI is conventionally defined by the normalized SLP difference between Tahiti and Darwin, while the PNA and NAO indices are defined with four action centers on the 500 hPa height (Wallace

and Gutzler 1981) and normalized SLP difference between Lisbon and Stykkisholmur (cf. Hurrell et al. t2003), respectively. These indices obtained from the LBM hindcast are imposed on the observed time series in Fig. 11. Since the tropical atmosphere is known to obey simpler linear dynamics, it is not surprising that the hindcast SOI has the correlation of 0.8 with the observed index (Fig. 11a). The interannual variations in PNA and NAO indices are more difficult to be reproduced, so that the correlation between the observed and hindcast time series is significant but not quite high: 0.36 for the PNA and 0.43 for the NAO (Fig. 11b,c). It is noteworthy that the LBM hindcast well reproduces the fluctuations in PNA and NAO during 1990s, as visible in Fig. 11b,c.

Figures 10 and 11 indicate that LBM captures, though not completely, a certain part of the extratropical atmospheric variability. Indeed, the leading EOFs to the SLP anomalies over the North Pacific and North Atlantic, respectively accounting for 29.6 and 31.9% of the total variance, are similar to the PNA and NAO patterns (not shown). Once the dominant teleconnection is identified in the hindcast, the linearity enables us to attribute the prevalence to the individual forcing. To examine the relative role of the diabatic heating and transient eddy forcing to the NAO, the SLP responses forced by one of them, together with the summation, are regressed upon the NAO index obtained from the hindcast (Fig. 12a-c).

The regressed SLP anomaly in the full hindcast (Fig. 12a) is quite similar to the observed NAO (cf. Hurrell et al. 2003) except for the midlatitude center less elongated toward the western North Atlantic. The SLP anomaly forced only by the transient eddies (Fig. 12b) has a strong projection onto the NAO-like pattern in Fig. 12a, especially over the northern part, while the counterpart forced only by the diabatic heating reveals a positive SLP regression over the southern part (Fig. 12c). Whether the thermally

induced response in Fig. 12c can modulate the Atlantic stork track such as to force the pattern in Fig. 12b, i.e., the possible positive feedback between the anomalous stationary eddies and transients, is beyond the scope of this study, but previous works support such a possibility (Peng and Whitaker 1999; Watanabe and Kimoto 2000; Peng and Robinson 2001; Pan et al. 2005).

It is interesting to regress with the model's NAO index not only of the hindcast response but also of the forcing, which clarifies the optimal forcing structure. The regressed pattern of the eddy vorticity forcing is somewhat noisy, though we can identify the positive vorticity source around Greenland and the negative source to the south (Fig. 12d), both of which will work to generate the NAO-like dipole circulation response. The regression of the diabatic heating (Fig. 12e) is more systematic in the tropics, indicating that the anomalous heating over the equatorial Indian Ocean and western Pacific, in addition to the heating over South America, is the major thermal forcing to the SLP anomalies shown in Fig. 12c. The connection between the heating anomaly (hence enhanced convections) over the tropical Indo-Pacific region and the positive NAO-like response is consistent with Hurrell et al. (2004), who showed that the recent positive NAO trend is attributed to the sea surface warming in the above region.

5. Summary and discussion

In a past decade, numerical studies on the climate variability tend to employ higher resolution GCMs. On the other hand, linearized atmospheric models, which have been shown to be relevant in delineating dynamical processes of the atmospheric anomalies, are yet used with a coarse resolution due to practical constraint of inverting the linear dynamical operator when solving steady forced responses with the zonally

asymmetric basic state. Motivated by the demand to solve the steady problem using LBM with satisfactory resolution, we attempted to propose an efficient method, called AIM in the present paper, based on a relaxation algorithm.

The primary idea of AIM is to decompose the linear operator matrix into a group of block matrices associated with the zonally uniform part of the basic state and a large matrix depending on the non-zonal part; the former can be easily inverted then the solution with the zonally uniform basic state is iteratively corrected by manipulating the latter. In general, such iteration does not converge for the dynamical equations of the atmosphere, so that an additional matrix ($\mathbf{R}$ in section 2a) is introduced not only to ensure the convergence but also to accelerate the iteration. The asymptotic convergence toward the true solution is accomplished by choosing $\mathbf{R}$ adequately which is controlled by a single parameter γ.

Efficiency of AIM is first tested with the linear barotropic model (section 3). It is shown that AIM is successful in obtaining the steady solution with quite small number of iteration. While the convergence rate is sensitive to the level of intrinsic diffusion of the system, it is more than one order faster than the other iterative method such as the time integration of the linear model. AIM is then applied to solve the steady response with LBM in section 4. Given the thermal and momentum forcing due to diabatic processes and transient eddies estimated from the observed data, LBM was shown to be capable of simulating the circulation anomalies during 1997/98 El Niño. Steady solutions were obtained in a similar manner for individual 43 winters during 1960-2002, composing the hindcast anomalies using LBM. Despite several discrepancies, the LBM hindcast shows the variance distribution of the northern extratropical height anomalies comparable to that observed, and reproduces a certain

fraction of the interannual variability in the dominant teleconnection patterns such as PNA and NAO; those indices based on the hindcast responses are significantly correlated with the observed indices.

AIM includes procedures for preparing and inverting the linear dynamical operator matrices for each zonal wavenumber with respect to the zonally asymmetric part of the basic state. The most efficient application of AIM would therefore be to solve a number of steady responses with the same basic state but different forcing, such as the hindcast presented in section 4b. Another potential application of AIM is a coupled atmosphere-ocean modeling using LBM. In particular, with slowly changing forcing associated with sea surface temperature, one can use the initial guess from the forced solution at previous step, so that only a few steps of iteration may be sufficient for convergence. This allows us to develop a very efficient coupled model with a slaved atmospheric component which may accommodate not only high resolutions but also other complexities much beyond Gill-type intermediate models. While the algorithm of AIM appears to be already efficient in the practical application, further acceleration may be possible by changing the definition of $\mathbf{R}$. We have examined the possibility, but currently not obtained a form of $\mathbf{R}$ better than Eq. (10), which remains to be the future issue.

While the LBM hindcast was able to simulate the dominant low-frequency variability to some extent, its reproducibility in terms of temporal fluctuation is not satisfactory (Fig. 11). This fail probably arises from an inaccuracy of the forcing terms. Since ERA40 data are provided on a linear grid at each pressure level, the forcing fields have to be interpolated both horizontally and vertically, resulting in the error increase. In particular, shallow heating over regions where surface pressure is above 1000 hPa

cannot be adequately estimated from the pressure level data. On the other hand, LBM forced by the forcing obtained from a GCM that shares the dynamical framework has been shown to yield better results in reproducing the low-frequency variability in the GCM (Ting and Lau 1993). We are currently testing the LBM hindcast, using AIM, of the GCM-generated anomalies, which will be reported elsewhere. There may be another cause as well: the boundary layer mixing represented by the uniform drag, which should vary in space depending on the stability and shear of the basic state (cf. DeWeaver and Nigam 2000).

As in the most of previous studies, steady atmospheric problem is solved in this study by prescribing the forcing due to diabatic processes and transient eddies. They are, however, partly dependent on the anomalous atmosphere, so that the LBM diagnosis is not actually closed. The ultimate goal of our linear atmospheric modeling is to construct a climate model that can be used as in the current LBM, by incorporating linearized moist schemes (Watanabe and Jin 2003) and a linear closure for the two-way feedback between transient eddies and low-frequency anomalies (Jin et al. 2005; Pan et al. 2005). For this purpose, we believe that AIM becomes a necessary and useful tool of solving the steady problems.

Acknowledgments. MW is supported by a Grant-in-Aid for Scientific Research from MEXT, Japan, and FFJ is supported by NOAA grants GC01-229 and GC01-246, NSF grants ATM-0226141 and ATM-0424799. This work was initiated during MW's visit at the Department of Meteorology, Florida State University in March 2005, when MW obtained the mathematical scheme of AIM designed by FFJ.

REFERENCES

Barnston, A. G., and R. E. Livezey, 1987: Classification, seasonality and persistence of low-frequency atmospheric circulation patterns. *Mon. Wea. Rev.*, **115**, 1083-1126.

Branstator, G., 1985: Analysis of general circulation model sea-surface temperature anomaly simulations using a linear model. Part I: Forced solutions. *J. Atmos. Sci.*, **42**, 2225-2241.

Branstator, G., 1990: Low-frequency patterns induced by stationary waves. *J. Atmos. Sci.*, **47**, 629-648.

Branstator, G., 1992: The maintenance of low-frequency atmospheric anomalies. *J. Atmos. Sci.*, **49**, 1924-1945.

DeWeaver, E., and S. Nigam, 2000: Zonal-eddy dynamics of the North Atlantic Oscillation. *J. Climate*, **13**, 3893-3914.

Greenbaum, A., 1997: *Iterative methods for solving linear systems.* In "Frontiers in Applied Mathematics", SIAM, 220pp.

Hall, N. M. J., and P. D. Sardeshmukh, 1998: Is the time-mean Northern Hemisphere flow baroclinically unstable? *J. Atmos. Sci.*, **55**, 41-56.

Held, I. M., M. Ting, and H. Wang, 2002: Northern winter stationary waves: Theory and modeling. *J. Climate*, **15**, 2125-2144.

Held, I. M., S. W. Lyons, and S. Nigam, 1989: Transients and the extratropical response to El Niño. *J. Atmos. Sci.*, **46**, 163-174.

Horel, J. D., and J. M. Wallace, 1981: Planetary-scale atmospheric phenomena associated with the Southern Oscillation. *Mon. Wea. Rev.*, **109**, 813-829.

Hoskins, B. J., and D. J. Karoly, 1981: The steady linear responses of a spherical atmosphere to thermal and orographic forcing. *J. Atmos. Sci.*, **38**, 1179-1196.

Hurrell, J. W., Y. Kushnir, G. Ottersen, and M. Visbeck, 2003: An overview of the North Atlantic Oscillation. In "*The North Atlantic Oscillation*", Hurrell, J. W., Y. Kushnir, G. Ottersen, M. Visbeck eds., *Geophysical Monograph*, **134**, 1-35.

Hurrell, J. W., M. P. Hoerling, A. Phillips, and T. Xu, 2004: Twentieth century North Atlantic climate change. Part I: Assessing determinism. *Clim. Dyn.*, **23**, 371-389.

Jin, F.-F., L.-L. Pan, and M. Watanabe, 2005: Dynamics of synoptic eddy and low-frequency flow interaction. Part I: A linear closure. *J. Atmos. Sci.*, revised.

Jin, F.-F., and B. J. Hoskins, 1995: The direct response to tropical heating in a baroclinic atmosphere. *J. Atmos. Sci.*, **52**, 307-319.

Kållberg, P., A. Simmons, S. Uppala, and M. Fuentes, 2004: The ERA-40 archive. ERA-40 Project Report Series, **17**, ECMWF, 31pp.

Kalnay, E., and Co-authors, 1996: The NCEP/NCAR 40-year reanalysis project. *Bull. Amer. Meteor. Soc.*, **77**, 437-471.

Kalnay, E., 2003: *Atmospheric modeling, data assimilation and predictability*. Cambridge University Press, 341pp.

Kushnir, Y., and J. M. Wallace, 1989: Low-frequency variability in the Northern Hemisphere winter: Geographical distribution, structure and time-scale dependence. *J. Atmos. Sci.*, **46**, 3122-3142.

Meurant, G., 1999: *Computer solution of large linear systems*. Elsevier, 776pp.

Navarra, A., 1990: Steady linear response to thermal forcing of an anomaly model with an asymmetric climatology. *J. Atmos. Sci.*, **47**, 148-169.

Pan, L.-L, F.-F Jin, and M. Watanabe, 2005: Dynamics of synoptic eddy and low-frequency flow interaction. Part III: Baroclinic model results. *J. Atmos. Sci.*, revised.

Peng, S., and J. S. Whitaker, 1999: Mechanisms determining the atmospheric response to midlatitude SST anomalies. *J. Climate*, **12**, 1393-1408.

Peng, S., and W. A. Robinson, 2001: Relationships between atmospheric internal variability and the responses to an extratropical SST anomaly. *J. Climate*, **14**, 2943-2959.

Ting, M., and I. M. Held, 1990: The stationary wave response to a tropical SST anomaly in an idealized GCM. *J. Atmos. Sci.*, **47**, 2546-2566.

Ting, M., and N.-C. Lau, 1993: A diagnostic and modeling study of the monthly mean wintertime anomalies appearing in a 100-year GCM experiment. *J. Atmos. Sci.*, **50**, 2845-2967.

Ting, M., and P. D. Sardeshmukh, 1993: Factors determining the extratropical response to equatorial diabatic heating anomalies. *J. Atmos. Sci.*, **50**, 907-918.

Ting, M., and L. Yu, 1998: Steady response to tropical heating in wavy linear and nonlinear baroclinic models. *J. Atmos. Sci.*, **55**, 3565-3582.

Wallace, J. M., 2000: North Atlantic Oscillation/annular mode: Two paradigms-one phenomenon. *Quart. J. R. Met. Soc.*, **126**, 791-805.

Wallace, J. M., and D. S. Gutzler, 1981: Teleconnections in the geopotential height field during the Northern Hemisphere winter. *Mon. Wea. Rev.*, **109**, 784-812.

Watanabe, M., and M. Kimoto, 2000: Atmosphere-ocean thermal coupling in the North Atlantic: A positive feedback. *Quart. J. R. Met. Soc.*, **126**, 3343-3369.

Watanabe, M., and M. Kimoto, 2001: Corrigendum. *Quart. J. R. Met. Soc.*, **127**, 733-734.

Watanabe, M., and F.-F. Jin, 2003: A moist linear baroclinic model: Coupled dynamical-convective response to El Niño. *J. Climate*, **16**, 1121-1139.

Watanabe, M., and F.-F. Jin, 2004: Dynamical prototype of the Arctic Oscillation as revealed by a neutral singular vector. *J. Climate*, **17**, 2119-2138.

Yanai, M., C. Li, and Z. Song, 1992: Seasonal heating of the Tibetan Plateau and its effects on the evolution of the Asian summer monsoon. *J. Meteor. Soc. Japan*, **70**, 319-351.

FIGURE AND TABLE CAPTIONS

Fig.1 RMS error ratio (ε) of the AIM solution as a function of the iteration step n. The error is computed by the T21 barotropic model with different values of γ.

Fig.2 Eigenvalue spectrum of $\mathbf{M}^*$ in the T42 barotropic model with (a) $\gamma = 0$ (equal to $\mathbf{M}$), (b) $\gamma = 1$, (c) $\gamma = 10$, and (d) $\gamma = 100$. σ_i and σ_r are the imaginary and real parts, respectively. A unit circle is drawn for reference.

Fig.3 As in Fig.1 but for ε calculated from three different methods: AIM with $\gamma = 4$, time integration, and conjugate gradient method. The 10% and 1% error levels are indicated by dashed lines. Note that three methods employ the same first guess.

Fig.4 Steady streamfunction response to the equatorial divergent forcing (denoted by shading) obtained from the T21 barotropic model. The contour interval is 1×10^6 m^2 s^{-1} while the negative contours are dashed. (a) True solution by the matrix inversion, (b) the AIM solution at n=1 with $\gamma = 4$, (c) the CG solution at n=262, and (d) the AIM solution at n=30. The RMS errors for (c) and (d) are 1%.

Fig.5 As in Fig.1 but for ε calculated with different magnitude of the diffusion, varying from 12hr to 2dy damping timescale for the smallest wave. The best value of γ employed in each computation is also indicated.

Fig.6 Number of iteration steps required for the convergence $\varepsilon \le 0.01$ in the barotropic model with different horizontal resolution. Dashed lines with circle, triangle, and cross show the solutions obtained from AIM, CG, and time integration, respectively, all employing the intrinsic diffusion common to the T21 resolution. Solid lines are the solutions with the diffusion dependent on the resolution (weaker in higher resolution,

following Table 1). The gray line indicates the number of degrees of freedom.

Fig.7 Differential norm ratio, λ, against the companion RMS error ratio, ε, for the AIM solutions in the barotropic model. The values are plotted up to n=70 for T21 while n=500 for the other resolution. The diffusion timescale for each resolution follows Table 1.

Fig.8 Anomalies of the 850 hPa wind (vector) and 300 hPa geopotential height (contour) (a) observed during winter 1997/98, and (b)-(c) obtained as a steady response to the observationally estimated forcing. The responses are calculated with T42 20-level LBM, under the zonally uniform basic state in (b) and 3D basic state in (c). The contour interval is 40 m for (a) while 30 m for (b)-(c), the zero contours omitted.

Fig.9 (a) Observed and (b) calculated SLP anomalies during winter 1997/98, the latter associated with the steady response shown in Fig. 8c. The contour interval is 2 hPa for (a) while 1 hPa for (b), the zero contours omitted. (c)-(d) As in (a)-(b) but for the temperature (contour, 1K interval) and height (shading) anomalies along 50°N. Topography resolved in LBM is presented by the black rectangles in (d).

Fig.10 Standard deviations of the 500 hPa height anomalies during 1960-2002, obtained from (a) ERA40, and hindcast response of T42 LBM (b) with the zonally symmetric and (c) zonally asymmetric basic states. The contour interval is 5m.

Fig.11 Observed (solid) and simulated (dashed) indices of the (a) Southern Oscillation, (b) PNA, and (c) NAO for winter 1960-2002. The simulated indices are obtained from the hindcast response of the T42 LBM.

Fig.12 (a) Steady hindcast response regressed upon the model NAO index, as represented by the SLP anomaly corresponding to the one standard deviation of the index. The contour interval is 0.3 hPa. (b)-(c) As in (a) but for the regression of the

hindcast forced only by the transient eddy vorticity fluxes and diabatic heating, respectively. (d) As in (b) but for the vertically averaged vorticity forcing. The contour interval is 1×10^{-6} s^{-1} day^{-1}. (e) As in (c) but for the vertically averaged heating. The contour interval is 0.2 K day^{-1}. The zero contours have been omitted and negative contours dashed in all the panels.

Table 1 Parameters used in the barotropic model with different horizontal resolution. The definitions of the RMS error ε and norm ratio λ are respectively given in Eqs. (11) and (12).

Table 1 Parameters used in the barotropic model with different horizontal resolution. The definitions of the RMS error ε and norm ratio λ are respectively given in Eqs. (11) and (12).

	T21	T42	T63	T106
Diffusion				
Order	4th	4th	4th	4th
Damping time	24hr	12hr	6hr	2hr
Best value of γ	4	38	77	200
Δt for time integration	60min	30min	20min	12min
n for ε=0.1	9	39	68	174
n for ε=0.01	30	106	211	404
λ for ε=0.1	0.093	0.057	0.043	0.044
λ for ε=0.01	0.006	0.006	0.003	0.004
Degrees of freedom	483	1848	4095	11448

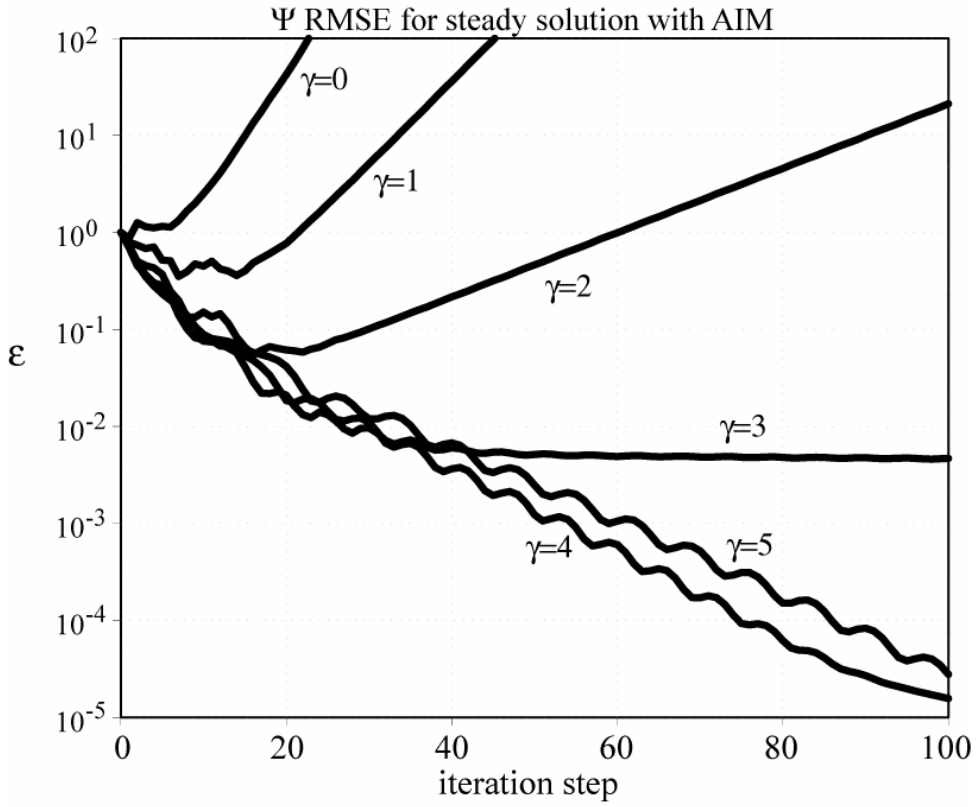

Fig.1 RMS error ratio (ε) of the AIM solution as a function of the iteration step n. The error is computed by the T21 barotropic model with different values of γ.

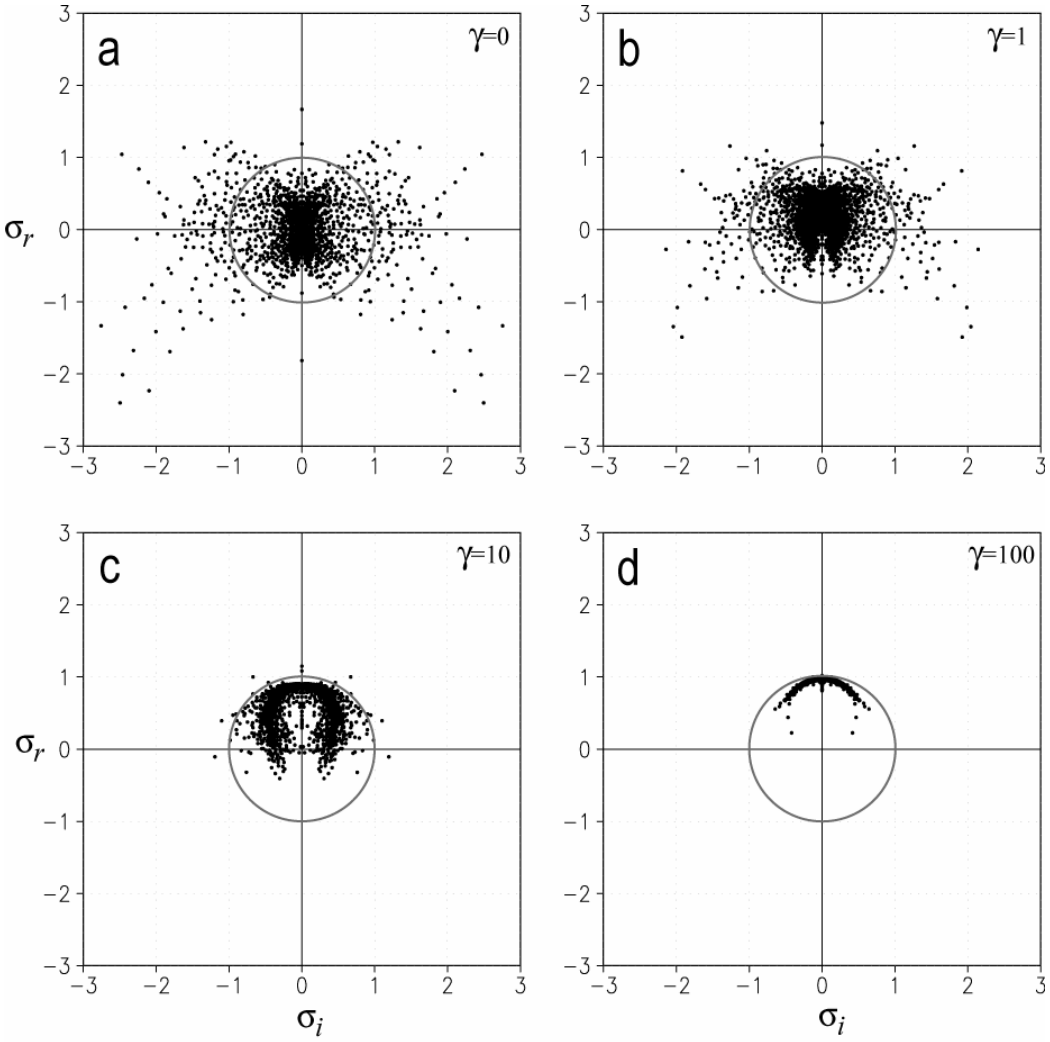

Fig.2 Eigenvalue spectrum of $\mathbf{M}^*$ in the T42 barotropic model with (a) $\gamma = 0$ (equal to $\mathbf{M}$), (b) $\gamma = 1$, (c) $\gamma = 10$, and (d) $\gamma = 100$. σ_i and σ_r are the imaginary and real parts, respectively. A unit circle is drawn for reference.

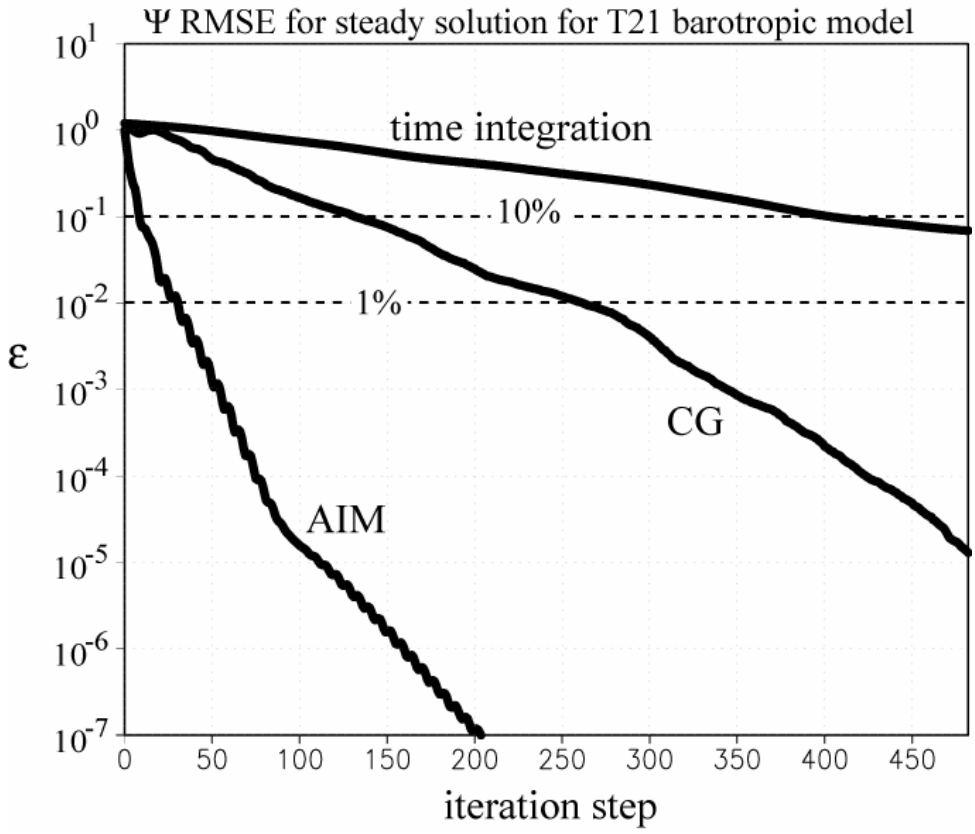

Fig.3 As in Fig.1 but for ε calculated from three different methods: AIM with $\gamma = 4$, time integration, and conjugate gradient method. The 10% and 1% error levels are indicated by dashed lines. Note that three methods employ the same first guess.

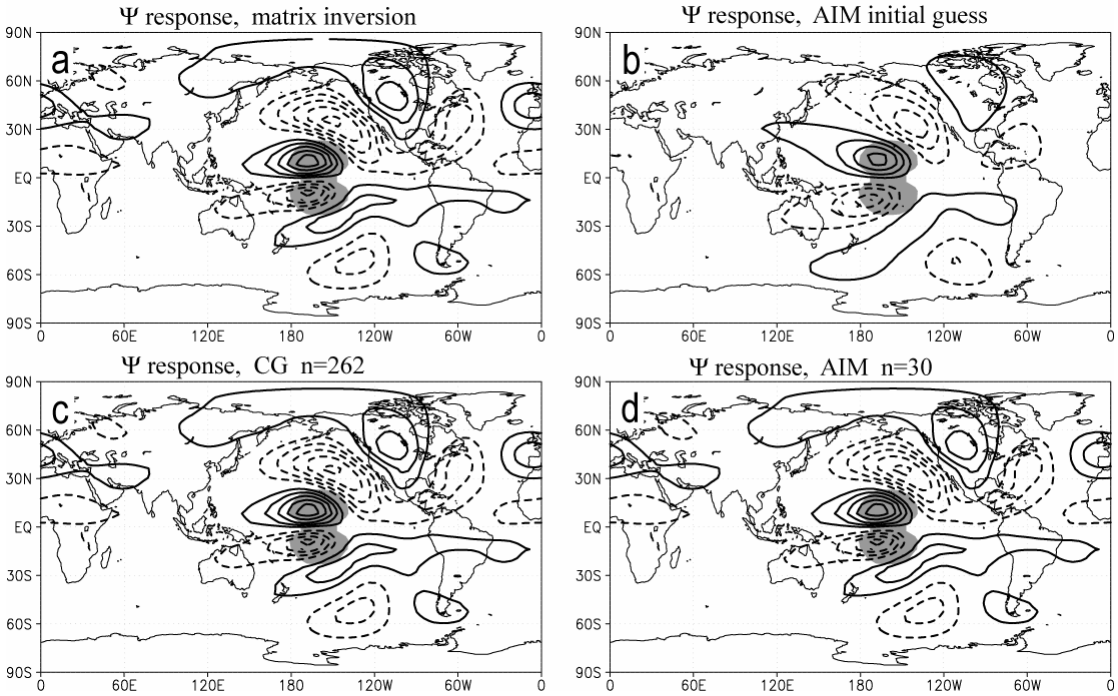

Fig.4 Steady streamfunction response to the equatorial divergent forcing (denoted by shading) obtained from the T21 barotropic model. The contour interval is 1×10^6 m^2 s^{-1} while the negative contours are dashed. (a) True solution by the matrix inversion, (b) the AIM solution at n=1 with $\gamma = 4$, (c) the CG solution at n=262, and (d) the AIM solution at n=30. The RMS errors for (c) and (d) are 1%.

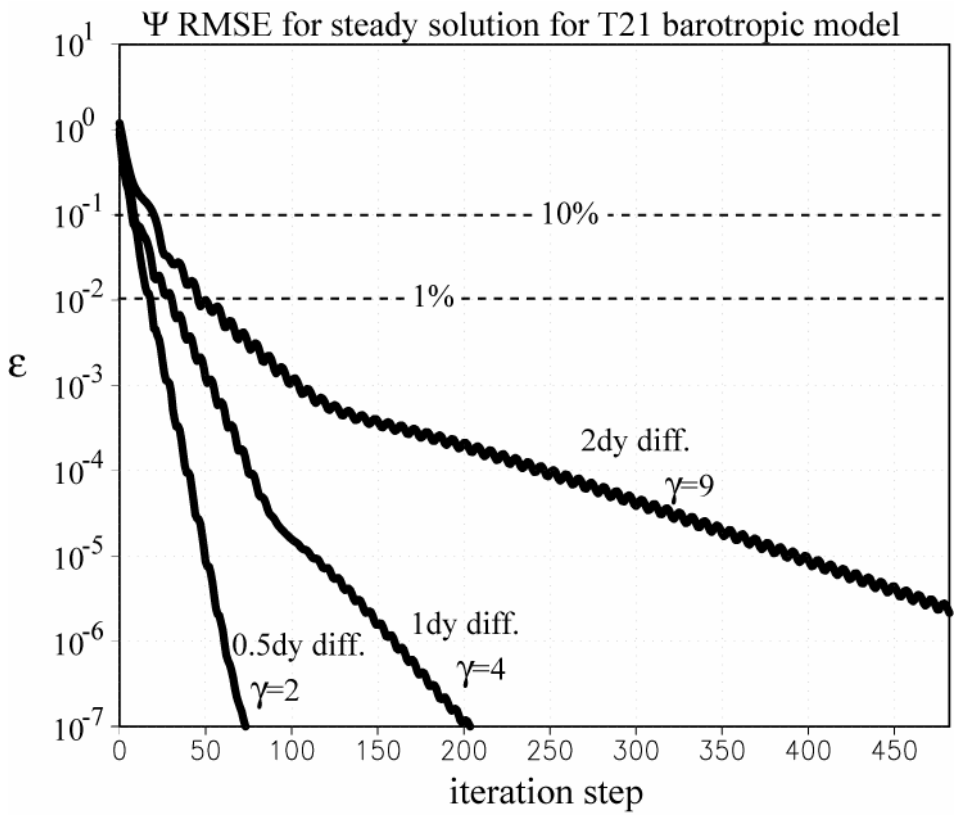

Fig.5 As in Fig.1 but for ε calculated with different magnitude of the diffusion, varying from 12hr to 2dy damping timescale for the smallest wave. The best value of γ employed in each computation is also indicated.

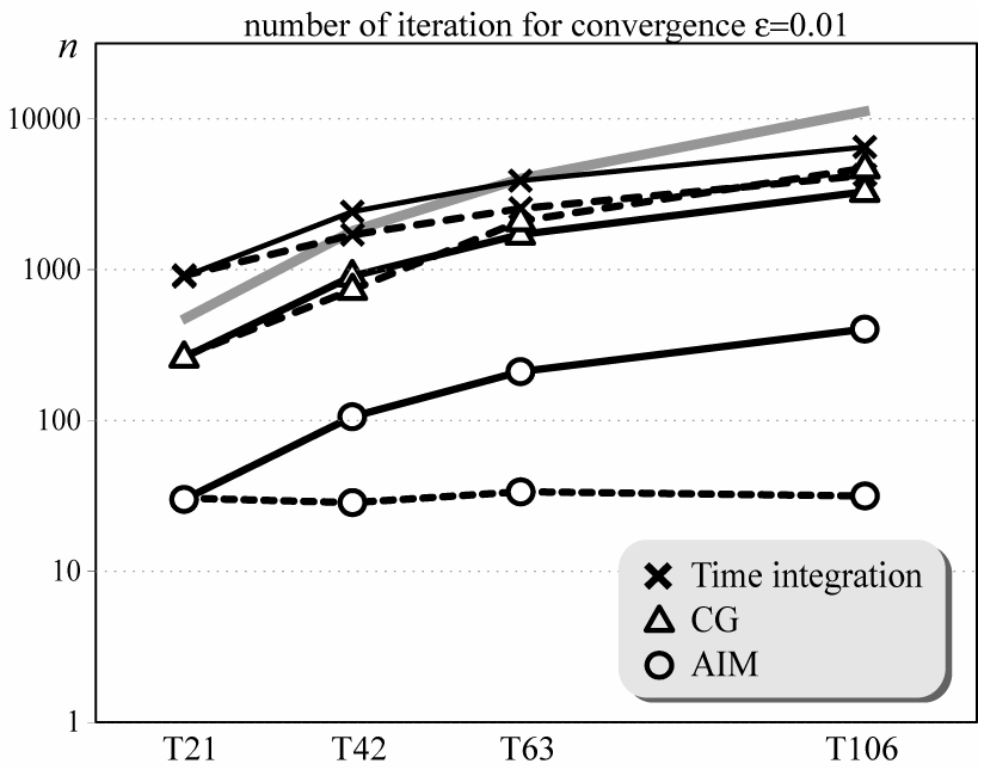

Fig.6 Number of iteration steps required for the convergence $\varepsilon \leq 0.01$ in the barotropic model with different horizontal resolution. Dashed lines with circle, triangle, and cross show the solutions obtained from AIM, CG, and time integration, respectively, all employing the intrinsic diffusion common to the T21 resolution. Solid lines are the solutions with the diffusion dependent on the resolution (weaker in higher resolution, following Table 1). The gray line indicates the number of degrees of freedom.

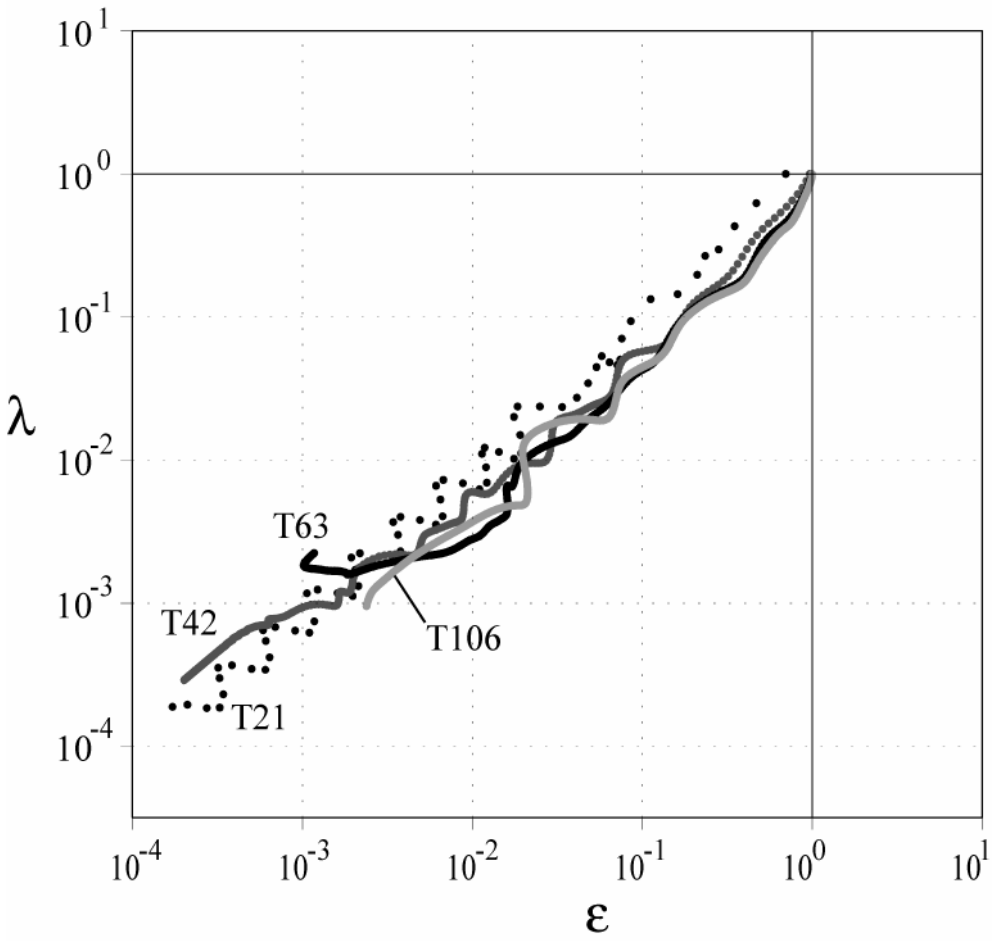

Fig.7 Differential norm ratio, λ, against the companion RMS error ratio, ε, for the AIM solutions in the barotropic model. The values are plotted up to n=70 for T21 while n=500 for the other resolution. The diffusion timescale for each resolution follows Table 1.

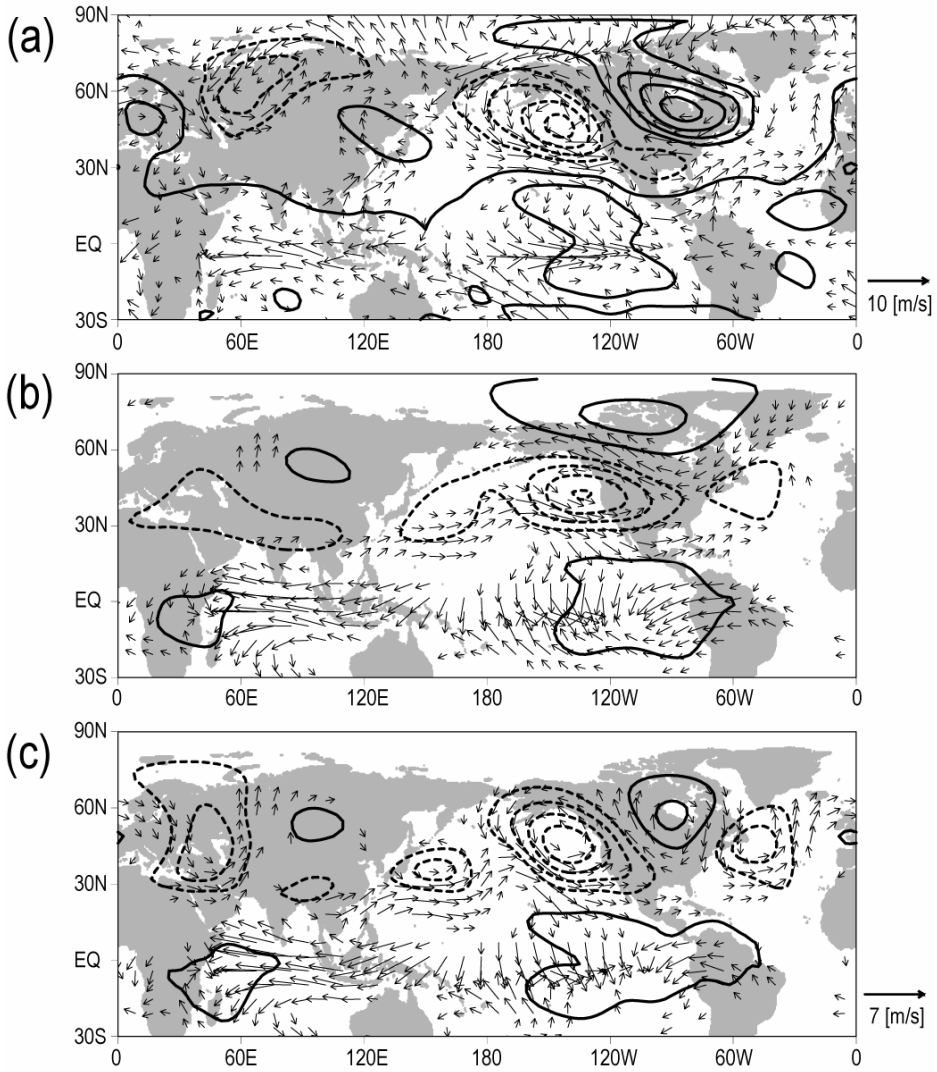

Fig.8 Anomalies of the 850 hPa wind (vector) and 300 hPa geopotential height (contour) (a) observed during winter 1997/98, and (b)-(c) obtained as a steady response to the observationally estimated forcing. The responses are calculated with T42 20-level LBM, under the zonally uniform basic state in (b) and 3D basic state in (c). The contour interval is 40 m for (a) while 30 m for (b)-(c), the zero contours omitted.

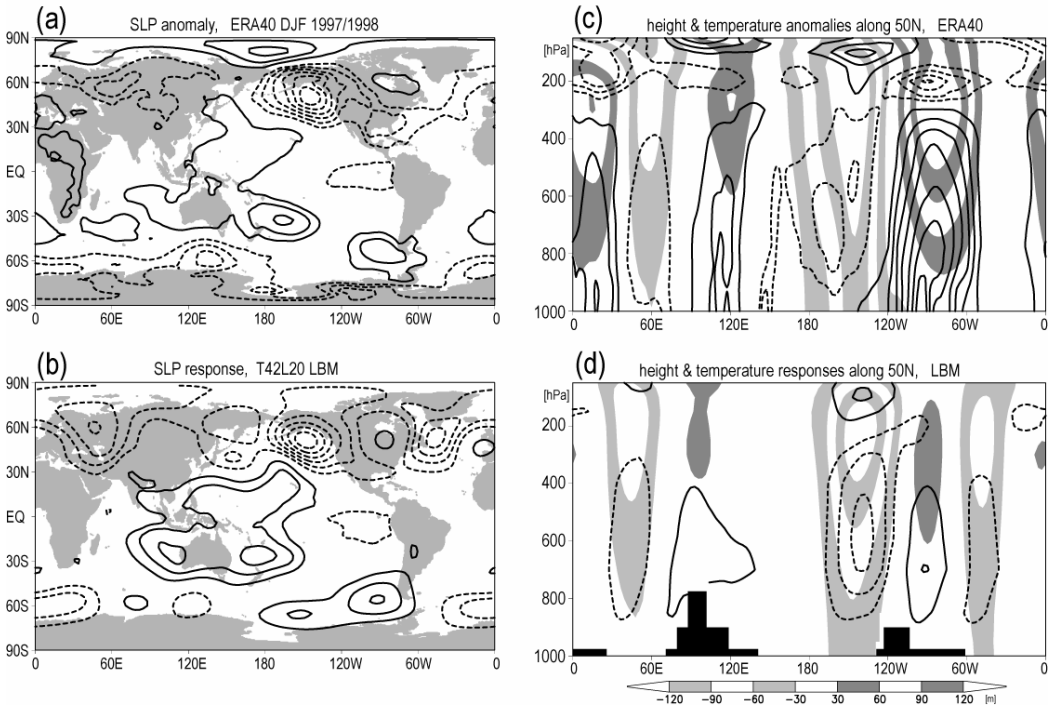

Fig.9 (a) Observed and (b) calculated SLP anomalies during winter 1997/98, the latter associated with the steady response shown in Fig. 8c. The contour interval is 2 hPa for (a) while 1 hPa for (b), the zero contours omitted. (c)-(d) As in (a)-(b) but for the temperature (contour, 1K interval) and height (shading) anomalies along 50°N. Topography resolved in LBM is presented by the black rectangles in (d).

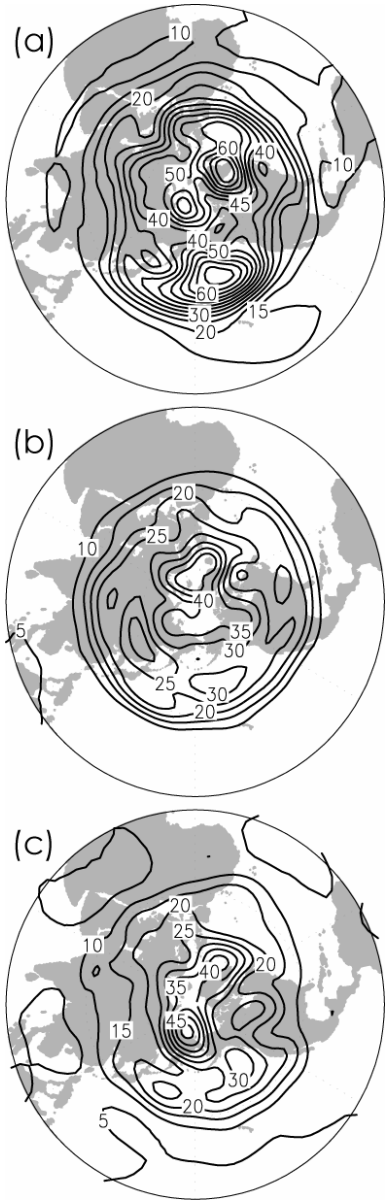

Fig.10 Standard deviations of the 500 hPa height anomalies during 1960-2002, obtained from (a) ERA40, and hindcast response of T42 LBM (b) with the zonally symmetric and (c) zonally asymmetric basic states. The contour interval is 5m.

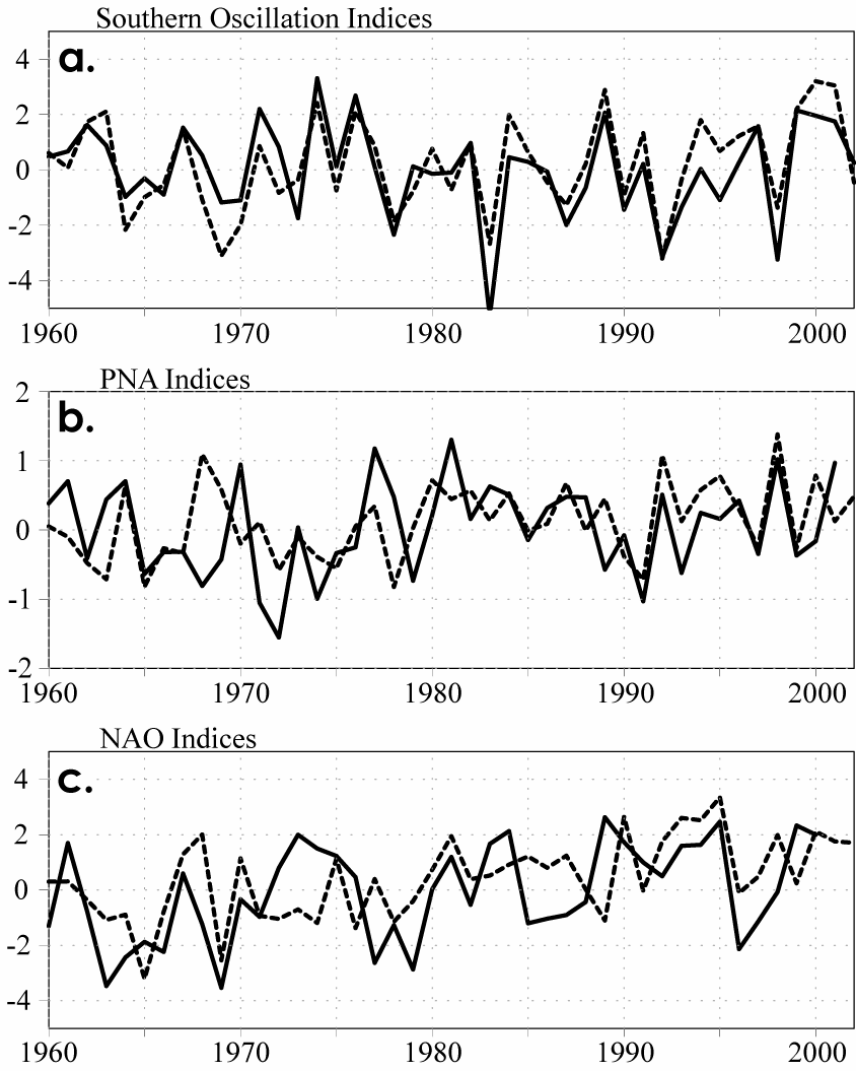

Fig.11 Observed (solid) and simulated (dashed) indices of the (a) Southern Oscillation, (b) PNA, and (c) NAO for winter 1960-2002. The simulated indices are obtained from the hindcast response of the T42 LBM.

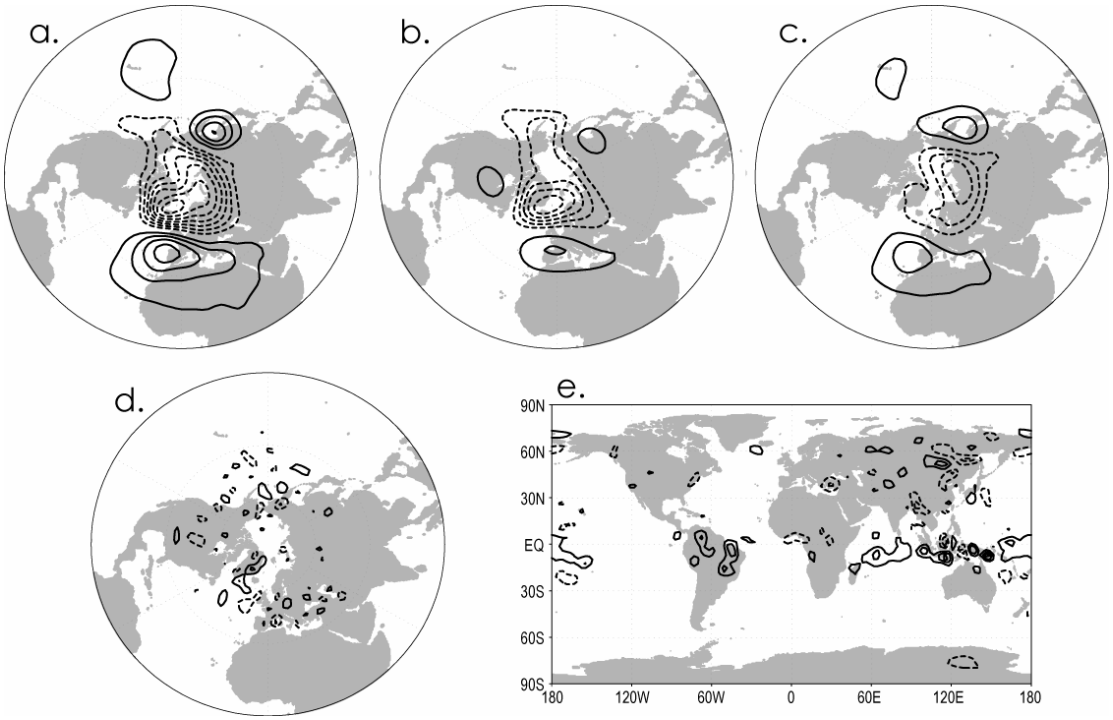

Fig.12 (a) Steady hindcast response regressed upon the model NAO index, as represented by the SLP anomaly corresponding to the one standard deviation of the index. The contour interval is 0.3 hPa. (b)-(c) As in (a) but for the regression of the hindcast forced only by the transient eddy vorticity fluxes and diabatic heating, respectively. (d) As in (b) but for the vertically averaged vorticity forcing. The contour interval is 1×10^{-6} s^{-1} day^{-1}. (e) As in (c) but for the vertically averaged heating. The contour interval is 0.2 K day^{-1}. The zero contours have been omitted and negative contours dashed in all the panels.